

Planetary Neutron Spectroscopy for Metal-rich Compositions: Development of Analysis Framework for Measurements at the Asteroid (16) Psyche

David J. Lawrence¹, John O. Goldsten², Patrick N Peplowski¹, Zachary W Yokley¹, Andrew W. Beck³, Morgan Burks⁴, Linda T. Elkins-Tanton⁵, Insoo Jun⁶, Timothy McCoy⁷, and Thomas H. Prettyman⁸

¹Johns Hopkins University Applied Physics Laboratory

²Unknown

³Marietta College

⁴Lawrence Livermore National Laboratory

⁵Arizona State University

⁶Jet Propulsion Lab (NASA)

⁷Smithsonian Institution

⁸Planetary Science Institute

November 22, 2022

Abstract

Neutron spectroscopy has become a standard technique for remotely measuring planetary surface compositions from orbital spacecraft around various planets. Measurements have successfully been carried out at the Moon, Mars, Mercury, and the asteroids Vesta and Ceres. The NASA Psyche mission is planning to make neutron measurements to characterize the composition of the M-class asteroid (16) Psyche. Earth-based remote sensing measurements allow for a wide range of Fe concentrations, ranging from ~25 wt.% to 90 wt.%, and geochemically plausible Ni concentrations range from 0 wt.% to 10 wt.% or higher. To prepare for the analysis of Psyche neutron data, we have developed a new principal component analysis framework using four neutron energy ranges of thermal, low-energy epithermal, high-energy epithermal, and fast neutrons. With this analysis framework, we have demonstrated that the neutron measurements can uniquely distinguish variations of metal-to-silicate fraction, Ni, and hydrogen compositions. The strongest principal component is that of metal-to-silicate; the second strongest is Ni variations; the third is hydrogen variations. The validity of this framework can be first tested during a Mars gravity assist prior to arrival at Psyche.

submitted to *Earth and Space Science*

1 **Planetary Neutron Spectroscopy for Metal-rich Compositions: Development of Analysis**
2 **Framework for Measurements at the Asteroid (16) Psyche**

3
4 David J. Lawrence, John O. Goldsten, Patrick N. Peplowski, and Zachary W. Yokley
5 *Johns Hopkins University Applied Physics Laboratory, Laurel, MD*

6
7 Andrew W. Beck
8 *Marietta College, Marietta, OH*

9
10 Morgan T. Burks
11 *Lawrence Livermore National Laboratory, Livermore, CA*

12
13 Linda Elkins-Tanton
14 *Arizona State University, Tempe, AZ*

15
16 Insoo Jun
17 *NASA Jet Propulsion Laboratory, Pasadena, CA*

18
19 Timothy J. McCoy
20 *Smithsonian Institution, Washington, DC*

21
22 Thomas H. Prettyman
23 *Planetary Science Institute, Tucson, AZ*

24
25
26 **Abstract**

27 Neutron spectroscopy has become a standard technique for remotely measuring planetary
28 surface compositions from orbital spacecraft around various planets. Measurements have
29 successfully been carried out at the Moon, Mars, Mercury, and the asteroids Vesta and Ceres. The
30 NASA Psyche mission is planning to make neutron measurements to characterize the composition
31 of the M-class asteroid (16) Psyche. Earth-based remote sensing measurements allow for a wide

32 range of Fe concentrations, ranging from ~25 wt.% to 90 wt.%, and geochemically plausible Ni
33 concentrations range from 0 wt.% to 10 wt.% or higher. To prepare for the analysis of Psyche
34 neutron data, we have developed a new principal component analysis framework using four
35 neutron energy ranges of thermal, low-energy epithermal, high-energy epithermal, and fast
36 neutrons. With this analysis framework, we have demonstrated that the neutron measurements can
37 uniquely distinguish variations of metal-to-silicate fraction, Ni, and hydrogen compositions. The
38 strongest principal component is that of metal-to-silicate; the second strongest is Ni variations; the
39 third is hydrogen variations. The validity of this framework can be first tested during a Mars
40 gravity assist prior to arrival at Psyche.

41

42 **1. Introduction**

43 Planetary neutron spectroscopy has become a standard technique for remotely measuring the
44 elemental composition of planetary surfaces from orbit. Neutrons are generated by nuclear
45 spallation reactions from galactic cosmic rays (GCRs) on airless or nearly airless planetary
46 surfaces. This technique was originally suggested by [Lingenfelter *et al.*, 1961], and measurements
47 of planetary neutrons were first accomplished with NASA's Lunar Prospector (LP) mission, which
48 separately measured thermal (neutron energy $E_n < 0.4$ eV), epithermal ($0.4 < E_n < \sim 10$ keV), and fast
49 ($E_n > 500$ keV) neutrons [Feldman *et al.*, 1998a; 1998b]. Subsequent neutron measurements have
50 been made at Mars [e.g., Feldman *et al.*, 2011; Maurice *et al.*, 2011], Mercury [e.g., Lawrence *et*
51 *al.*, 2013a; Lawrence *et al.*, 2017], and the asteroids Vesta and Ceres [e.g., Prettyman *et al.*, 2012;
52 2017].

53 Compositional information of planetary surfaces is acquired via different energy ranges of the
54 leakage neutrons. The lowest energy range (thermal neutrons) provides sensitivity to variations in
55 strongly neutron-absorbing elements. On typical planetary surfaces, major elements that are strong
56 neutron absorbers include Fe and Ti [Feldman *et al.*, 1998a]. Minor elements that are strong
57 neutron absorbers are Cl and Ni, and these elements can affect thermal neutron measurements
58 when they have sufficiently high concentrations (e.g., Mars, Psyche). Finally, there are trace rare-
59 earth elements (e.g., Gd and Sm) that cause thermal-neutron variations when these elements have
60 concentrations of tens of ppm [Elphic *et al.*, 2000].

61 Medium energy neutrons (or epithermal neutrons) primarily have sensitivity to variations in
62 hydrogen (H) due to the strong neutron moderation that occurs with H. Depending on the sensors

63 used for detection, epithermal neutrons are also sensitive to variations in rare-earth elements
64 [Lawrence *et al.*, 2006]. The highest energy range (or fast neutrons) has sensitivity to variations
65 in average atomic mass ($\langle A \rangle$). On typical planetary surfaces, the elemental variations that drive
66 fast-neutron variability are generally Fe, Al, Mg, and O [Lawrence *et al.*, 2017]. For large H
67 concentrations ($>$ few hundred parts per million [ppm]), fast neutrons show variations due to
68 neutron moderation and are sensitive to depth variations of H concentrations up to tens of cm
69 [Feldman *et al.*, 2007].

70 The NASA Psyche mission to the asteroid (16) Psyche broadens the expected phase space of
71 neutron measurements with the possibility of very high Fe abundances (up to 90 wt.%) and up to
72 \sim 10 wt.% or greater Ni [Elkins-Tanton *et al.*, 2020]. Such high metal abundances will significantly
73 affect the leakage neutron flux and therefore require a new assessment of how to carry out and
74 interpret neutron data. Additionally, the Psyche neutron spectrometer will separately sample four
75 different neutron energy bands, providing a larger dataset than has been collected by prior neutron
76 spectroscopy investigations. Towards this end, we present a new analysis framework where the
77 different compositional variabilities expected on Psyche can be identified and quantified. For this
78 study, we provide an overview of possible Psyche compositions and how they relate to neutron
79 spectroscopy measurements (Section 2); provide a summary of the planned Psyche neutron
80 measurements (Section 3); and finally, present simulated neutron fluxes, predicted neutron count
81 rates, and a principal component analysis framework that can be used to analyze and interpret the
82 expected Psyche neutron data (Section 4).

83

84 **2. Possible (16) Psyche Composition: Elements Relevant to Neutron Spectroscopy**

85 One of the primary science objectives of the Psyche mission is to measure the asteroid Psyche's
86 elemental composition to determine if it is a remnant core of a protoplanetary body [Elkins-Tanton
87 *et al.*, 2020]. To accomplish this objective, the mission includes a Gamma-Ray and Neutron
88 Spectrometer (GRNS) that will measure Psyche's elemental composition for a number of elements
89 (Fe, Ni, Si, K, Al, Ca, and S) using a Gamma-Ray Spectrometer (GRS), and will measure
90 complementary compositional parameters using a Neutron Spectrometer (NS) [Lawrence *et al.*,
91 2019].

92 A key goal of the Psyche neutron measurements is to quantify the asteroid metal-to-silicate
93 fraction. When discussing "metal-to-silicate fraction" for gamma-ray and neutron spectroscopy,

94 an important distinction needs to be understood. For typical meteorite science investigations,
95 metal-to-silicate fraction is defined as the total amount of metal (e.g., metallic iron and nickel)
96 versus total silicates (elements bound as oxides). Thus, in the standard geochemical definition,
97 oxidized iron (e.g., FeO) is “book kept” with silicates. In contrast, gamma-ray and neutron
98 spectroscopy is sensitive elemental composition independent of the material’s mineralogical state.
99 For Psyche, the largest concentration of “metal” elements being considered consist of Fe and Ni;
100 we therefore define the “metal” content as the total concentration of Fe and Ni, regardless of its
101 mineral host. Silicates are defined as materials containing other major rock-forming elements (Si,
102 O, Al, Mg, Ca, etc.). The silicate fraction as defined here is a compositional parameter that can be
103 specified for any mixture of minerals (see Table 2) and determined using neutron spectroscopy.

104 On typical planetary bodies, the elements that primarily affect neutron measurements are Fe,
105 Ti, Cl, Ni, Gd, Sm, and H, as well as elements with contrasting $\langle A \rangle$ (see Section 1). Recent Earth-
106 based measurements and new interpretations of existing measurements have revised our
107 understanding of the nature of Psyche, and the currently accepted density of Psyche is bounded to
108 be 3.4–4.1 g/cm³ [Elkins-Tanton *et al.*, 2020]. Psyche’s Fe abundances could plausibly range from
109 25 wt.% to upwards of 90 wt.%, and by consequence, the silicate fraction could range from less
110 than 0.1 to greater than 0.7. Meteoritic analogs for Psyche therefore include iron meteorites as
111 well as metal-rich meteorites such as CB and enstatite chondrites, pallasites, and mesosiderites
112 [Peplowski *et al.*, 2019]. If Psyche is related to iron meteorites, then it must have significantly
113 higher porosity than is typical for >100-km-diameter asteroids, or retain a significant fraction of
114 the silicate shell, given the relatively low density. The wide range of compositions suggest that
115 additional elements including Mg, C, P, and Co, may be geochemically important [Peplowski *et*
116 *al.*, 2019] and thus we include them when modeling expected neutron fluxes.

117 Another element that has gained increased importance at Psyche is H. Ground-based
118 measurements using the NASA Infrared Telescope Facility have detected a 3- μ m absorption on
119 Psyche that is consistent with hydration features attributed to OH and H₂O bearing phases [Takir
120 *et al.*, 2017]. By analogy to the basaltic asteroid 4 Vesta [Prettyman *et al.*, 2012], this H may be
121 due to exogenous, water-rich carbonaceous-chondritic material accumulated on its surface. Based
122 on a cross correlation of Earth-based data from both Vesta and Psyche with orbital H
123 measurements at Vesta, Reddy *et al.* [2018] estimated that the bulk hydrogen concentrations could
124 be in the range of 200 – 300 ppm, which is comparable to the range of H variations (0 – 400 ppm)

125 seen at Vesta [Prettyman *et al.*, 2012; Lawrence *et al.*, 2013b]. While not needed to directly
126 address the mission’s science objectives, H in this abundance range can affect the measured
127 neutron composition parameters [Lawrence *et al.*, 2013b; Prettyman *et al.*, 2013], as well as
128 gamma-ray data when making composition measurements using both capture and inelastic
129 gamma-ray lines [Yamashita *et al.*, 2013; Peplowski *et al.*, 2015a; Wilson *et al.*, 2019]. Thus,
130 effects from bulk H concentrations and its possible spatial variability need to be taken into account
131 with the measured GRNS data.

132

133 3. The Psyche GRNS and Neutron Flux Environment at Psyche

134 The Psyche GRNS consists of two sensor subsystems that separately measure gamma rays
135 and neutrons [Lawrence *et al.*, 2019]. The GRS uses a cryocooled high-purity Ge (HPGe) sensor
136 to measure gamma rays with high precision and excellent energy resolution (≤ 3.5 keV @ 1332
137 keV). The HPGe sensor is surrounded by a borated plastic scintillator anticoincidence (AC) shield
138 that both provides active background rejection from charged particles for the gamma-ray
139 measurements, as well as fast-neutron measurements due to its 5 wt. % boron loading. As with
140 the MESSENGER GRS [Peplowski *et al.*, 2015b], the AC shield has a solid “puck” (7.75 cm
141 radius and 5.76 cm tall) and cylindrical annulus (1.75 cm thick and 8.8 cm tall). The NS consists
142 of three, identical ^3He gas proportional sensors (5.08-cm diameter, 25.41-cm long active length,
143 10-atmosphere pressure)[Peplowski *et al.*, 2020] that use different material coverings to
144 discriminate three separate neutron energy ranges (Figure 1). Thermal and low-energy epithermal
145 neutrons are measured using a bare sensor and a 0.05 cm-thick Cd-covered sensor; high-energy
146 epithermal (~ 1 keV $< E_n < 500$ keV) neutrons are measured with a polyethylene-covered (1-cm
147 thick) ^3He sensor. As a consequence, the term “neutron sensors” includes the NS subsystem, along
148 with the borated plastic scintillator from the GRS subsystem.

149 The energy-dependent response of the neutron sensors is shown in Figure 2. The lowest energy
150 thermal neutrons are detected with two ^3He sensors, as was done for the Lunar Prospector mission
151 [Feldman *et al.*, 2004]. The bare ^3He sensor detects the combined flux of thermal plus epithermal
152 neutrons, and the Cd-covered ^3He sensor detects epithermal neutrons. The Cd-covered sensor uses
153 a 0.05-cm-thick layer of Cd, which absorbs all neutrons with energies less than 0.4 eV. Thermal
154 neutrons are thus measured as the count-rate difference between the bare and Cd-covered sensors.
155 The third sensor is covered in a 1-cm-thick layer of polyethylene to increase sensitivity for high-

156 energy-epithermal neutrons. Detection of high-energy-epithermal neutrons is used to optimize
157 neutron measurements at Psyche to account for the possibly higher Fe and Ni content than any
158 other planetary body for which neutron measurements have been made, as well as variable H
159 concentrations.

160 A very high metal content (up to 90 wt.% Fe) will significantly modify the emitted neutron
161 flux compared to bodies with rocky silicate-rich materials. Modeled neutron fluxes for various
162 permutations of metal-to-silicate fractions and H concentrations are shown in Figure 3. When the
163 metal fraction is increased (Figure 3A), the thermal neutron flux is suppressed, and the high-energy
164 neutron flux is enhanced. Thermal neutrons are suppressed because both Fe and Ni are highly
165 efficient absorbers of thermal neutrons. The microscopic neutron absorption cross sections (at
166 0.025 eV) for the most abundant Fe and Ni isotopes ^{56}Fe and ^{58}Ni are 2.6 and 4.2 barn (10^{-24} cm^2),
167 respectively. These values compare to neutron absorption cross sections that range from 10^{-4} to
168 0.6 barn for other common elements in silicate materials (e.g., O, Si, Al, Ca, Mg). The fluxes of
169 high-energy epithermal and fast neutrons are correspondingly enhanced for increasing metal
170 content because for both energy ranges, larger neutron fluxes are generated for materials with
171 larger average atomic mass ($\langle A \rangle$) [Gasnault *et al.*, 2001; Lawrence *et al.*, 2011]. The largest
172 metal-to-silicate fractions considered for possible Psyche-like materials have $\langle A \rangle$ values around
173 ~ 40 – 50 atomic mass units (amu), compared to ~ 20 – 25 amu for typical silicate materials. It should
174 be noted that because the per-nucleon-binding energy of Ni is higher than Fe, the neutron
175 separation energy is likewise higher and thus liberation of neutrons during nuclear spallation of Ni
176 is inhibited, relative to Fe [Peplowski *et al.*, 2018]. Thus, for materials with large Ni
177 concentrations, there will be a breakdown of the well-known correlation between fast neutron
178 production and average atomic mass [Gasnault *et al.*, 2001].

179 In addition to metal content, variable H concentrations will cause neutron-flux changes that
180 need to be considered when analyzing and understanding the neutron data. As mentioned in
181 Section 2, H is likely present on Psyche at hundreds of ppm [Reddy *et al.*, 2018] and possibly has
182 variable concentrations across its surface [Sanchez *et al.*, 2017]. Typically, H is measured using
183 the low-energy portion of epithermal neutrons ranging from 0.3 eV to ~ 1 – 10 keV [Feldman *et al.*,
184 1998b]. For metal-rich compositions with varying H concentrations, this low-energy epithermal
185 energy range has little sensitivity to H concentrations, and the energies sensitive to H are shifted
186 to higher energies of 10 keV to a few hundred keV (Figure 3B). Thus, while the Cd-covered ^3He

187 neutron sensor provides the needed background subtraction for the bare ^3He sensor, it will not
188 provide a sensitive measure of H concentrations for a metal-rich body. The polyethylene covered
189 ^3He sensor provides an order-of-magnitude increased sensitivity to high-energy epithermal
190 neutrons (Figure 2) compared to either the bare or Cd covered sensors.

191

192 **4. Deriving Compositional Variations with Psyche Neutron Data**

193 The Psyche GRNS provides four neutron measurables of thermal, low-energy epithermal,
194 high-energy epithermal, and fast neutrons. Here, we describe particle transport simulations to
195 estimate the performance of these neutron measurements for a range of plausible Psyche
196 compositions. The neutron production was simulated by illuminating a Psyche sized body with a
197 GCR proton flux using the particle transport code MCNPX, which has a long history of application
198 for planetary nuclear spectroscopy applications [e.g., *Prettyman et al.*, 2006]. Using the sensor
199 energy-dependent responses shown in Figure 2, simulations were carried out to calculate the
200 expected neutron count rates for a range metal-to-silicate ratios, Ni concentrations, and H
201 concentrations. Metal concentration ranged from 10 to 90 vol.% metal in steps of 10 vol. %; Ni
202 abundances ranged from 2 wt.% to 30 wt.% Ni in steps of 2 wt.%; and H abundances ranged from
203 0 to 500 ppm H in steps of 100 ppm. Metal is nominally defined using IVA iron-meteorite
204 composition with 8.4 wt.% Ni, the remainder Fe, and silicates are defined as Mg-rich
205 orthopyroxene (bronzite -- $\text{Mg}_{0.87}\text{Fe}_{0.13}\text{SiO}_3$), as has been predicted to exist on Psyche [*Hardersen*
206 *et al.*, 2005]. Bulk compositions from various vol.% fractions of metal and bronzite were
207 calculated using modal recombination analysis [*Berlin et al.*, 2008], thus accommodating for the
208 large density contrast between metal and silicate. While the silicate ($\text{Mg}_{0.87}\text{Fe}_{0.13}\text{SiO}_3$)
209 contribution to Fe_{total} is insignificant with moderate or high vol.% metal, when metal becomes very
210 low in concentration, we acknowledge that Fe_{total} would largely be controlled by silicate
211 composition.

212 In total, 840 simulated neutron spectra were calculated from which neutron count rates were
213 derived. In order to approximate the expected measured count rates at Psyche, the modeled count
214 rates from the bare and Cd-covered ^3He sensors were scaled to the measured and modeled count
215 rates from the similar sensors from the LP-NS using a lunar highlands material [*Lawrence et al.*,
216 2006], accounting for differences in geometry between the lunar measurements and those planned
217 for Psyche's low-attitude mapping orbit. The count rates for the polyethylene covered ^3He sensor

218 were obtained by scaling the relative energy-integrated responses of the polyethylene- and Cd-
219 covered ^3He sensors. The count rates for the fast neutron sensor were obtained by scaling the
220 count rate from the MESSENGER NS fast neutron sensor at Mercury [Lawrence *et al.*, 2013a;
221 2017], which has a similar size to the Psyche GRS borated plastic scintillator. The count rates
222 were scaled to an assumed altitude of one Psyche radius. A full understanding and calibration of
223 all the neutron sensors will be obtained after the complete instrument calibration measurements
224 are completed. Additional benchmarking and calibration will be accomplished using flight data
225 from the Mars gravity assist.

226 Figure 4 shows count-rate plots for the six different permutations of thermal, low-energy
227 epithermal, high-energy epithermal, and fast neutrons. In each plot, lines of constant metal-to-
228 silicate fraction and constant Ni are given by the red and black lines, respectively. The red/black
229 contours show the count rates for 0 ppm H; the gray contours show count rates for 500 ppm H.
230 Each sensor combination provides different information about the three composition measurables
231 of metal-to-silicate fraction (or silicate fraction), Ni abundances, and H abundances. For example,
232 the combination of thermal versus fast neutrons (Figure 4A) provides a good measure of silicate
233 fraction. Specifically, high thermal and low fast neutron count rates indicate a high silicate
234 fraction, and the reverse (low thermal and high fast neutron count rates) indicate low silicate
235 fraction. This behavior is also clearly observed in the neutron fluxes given in Figure 3A. However,
236 with variable and/or uncertain H abundances, the thermal versus fast neutron count-rate
237 combination would do a poor job of constraining Ni concentrations, as there is significant overlap
238 for count rates with variable H abundances. In contrast, the combination of fast versus high-energy
239 epithermal neutrons (Figure 4B) can provide constraints on both silicate fraction and Ni
240 abundances for variable H abundances, although there are still ambiguities. While we do not go
241 into detail for the other measurement combinations, it is clear that each combination can provide
242 some constraints on the compositional measurements, but also suffer from various ambiguities.

243 To simplify our understanding of this complex phase space of four neutron measurements and
244 three compositional variables, we use an analysis technique known as Principal Component
245 Analysis (PCA). PCA is a statistical technique where a set of partially correlated measurements –
246 in this case the four neutron measurements – undergo a geometric-like transformation to generate
247 a new set of variables that are formally uncorrelated. While one of the major benefits to PCA
248 operations is to reduce the number of “important” variables, in this case PCA is used to maximize

249 compositional information while minimizing ambiguous overlap of measured data. Background
250 information on PCA can be found in many places; a good overview is provided in [Wilks, 2011].
251 In addition, PCA has been used in a variety of planetary nuclear spectroscopy studies [Chevrel et
252 al., 2002; Beck et al., 2015; Peplowski and Stockstill-Cahill, 2019].

253 For our purposes, we define a measurement vector $\mathbf{x} = [C_{\text{therm}}, C_{\text{lowE}}, C_{\text{highE}}, C_{\text{fast}}]$, where C
254 represents the simulated count rates for each GRNS neutron sensor. The PCA was carried out
255 using the *pcomp* function that is a part of the Interactive Data Language analysis package. The
256 input to the function is a 4 x 840 element array of data vectors (\mathbf{x}_m , where m ranges from 0 to 839)
257 that represents each of the 840 count-rate simulations (e.g., Figure 4). Using these input values,
258 the *pcomp* function outputs a 4 x 4 element matrix, \mathbf{E} , that transforms each input data vector into
259 a new principal component (PC) vector, \mathbf{u} :

260

$$261 \quad \mathbf{u}_m = \mathbf{E}\mathbf{x}_m \quad (1)$$

262

263 In addition, the *pcomp* function outputs a four-element variance vector that quantifies the
264 percentage of the total dataset variation (or weighting) for each principal component (PC) variable.
265 One way to intuitively understand this PC process is that as in standard linear algebra or quantum
266 mechanics, the PCs are eigenvectors, and their weighting values are the eigenvalues.

267 Results of the PCA are shown in Table 1 and Figure 5. Starting with Table 1, the first column
268 shows the percentage variance contained in each PC. PC1 dominates the total variance at 95%,
269 and the next two variables, PC2 and PC3, have variances comparable with each other at 3.5% and
270 1.1%, respectively. PC4 has a variance that is a factor of 18 lower than PC3. Thus, this PCA
271 shows that over 99% of the variance in the four neutron measurables can be represented by only
272 three PCs. The last four columns in Table 1 show the transformation matrix \mathbf{E} , such that each row
273 indicates how each PC is a linear combination of all four neutron measurables. For example, the
274 largest contributor to PC1 is the fast-neutron count rate with a coefficient of 0.865 followed by the
275 thermal neutron count rate of -0.384. The positive fast-neutron coefficient indicates that the PC1
276 parameter increases when the fast-neutron count rate increases, and the negative thermal-neutron
277 coefficient indicates that the PC1 parameter decreases when the thermal-neutron count rate
278 increases. As is seen below, this is consistent with the observation that PC1 is strongly correlated
279 with the silicate fraction compositional parameter. We also note that all neutron measurables have

280 a non-negligible contribution to PC1, thus indicating that all neutron measurements are needed to
281 derive PC1.

282 Figure 5 shows three-dimensional scatter plots where each of the 840 x 4 element vectors have
283 been transformed into PC space. The resulting data cloud is a stretched and curved parallelepiped-
284 like volume. Most importantly, there are no overlapping data points as each is located in a unique
285 position within the volume. To illustrate the compositional variability within this PC volume, each
286 panel shows the data points color coded to represent the silicate fraction (Figure 5A), the Ni
287 concentration (Figure 5B), and the hydrogen concentration (Figure 5C). PC1 is dominantly
288 correlated with silicate fraction, PC2 is dominantly correlated with Ni concentration, and PC3 is
289 dominantly correlated with H concentration. Thus, with an appropriate calibration, each of the
290 PCs can be directly linked to a specific composition parameter.

291 The variations of the different PCs can be understood in terms of the elemental variations in
292 the following manner. First, PC1, which positively correlates with silicate fraction, has an
293 anticorrelation with thermal, low-energy, and high-energy epithermal neutrons; whereas it has a
294 positive correlation with fast neutrons. This makes sense such that the neutron absorption due to
295 the metal elements (Fe, Ni) cause the count rates from the three lowest energy bands to decrease
296 (Note, even the high-energy epithermal-neutron sensor has a substantive response to low-energy
297 neutrons where there is strong neutron absorption). In contrast, fast neutrons, which show
298 increased count rates for larger metal count rates, has a strong positive correlation (0.865) with
299 PC1. Second, PC2, which correlates with Ni abundances (Figure 5B), anticorrelates with all
300 neutron measurables. These anticorrelations (especially the -0.817 value for thermal neutrons),
301 makes sense because the low-energy neutron absorption for Ni is ~60% stronger than for Fe, the
302 other metal constituent (Section 3). The negative correlations for fast, and possibly high-energy
303 epithermal neutrons are likely due to the fact that neutron spallation from Ni is inhibited compared
304 to the spallation from Fe [Peplowski *et al.*, 2018]. Finally, PC3, which negatively correlates with
305 hydrogen abundances, has the strongest correlation with high-energy epithermal neutrons (0.838)
306 as well as positive correlations with low-energy and fast neutrons. This indicates that as the
307 hydrogen concentration goes up, the three highest-energy neutron measurements decrease, which
308 is consistent with the fluxes shown in Figure 3B. In contrast, for increasing hydrogen content
309 (decreasing PC3), the thermal neutrons increase, which is again consistent with Figure 3B.

310 While the PCA appears to be useful in interpreting these simulated neutron data, we recognize
311 that these count rates were generated using an “artificial” bulk compositional framework, i.e., we
312 used compositions that span the large ranges of silicate fraction, Ni and H concentrations, but we
313 did not replicate the compositions of any specific meteorite or rock type. To test how this analysis
314 framework represents known compositions, we calculated neutron fluxes for six different bulk
315 meteoritic compositions. These are meteoritic compositions identified by *Peplowski et al.* [2019]
316 and *Elkins-Tanton et al.* [2020] as spanning the likely possible values that will be observed at
317 Psyche. The compositional values are given in Table 2 along with the associated silicate fractions.
318 Figure 5D shows these count rates transformed into PC space. The PC values for these meteorite
319 compositions are also given in Table 3. As seen, the PC1 values for these meteoritic compositions
320 correlate closely with silicate fraction. This correlation is seen more clearly in Figure 6A where
321 the PC1 value is plotted versus silicate fraction for the six meteoritic compositions. Variations in
322 Ni abundances also track with PC2, which is more clearly seen in Figure 6B. We note, however,
323 that since the contours of increasing Ni abundances are not strictly parallel to PC2, the correlation
324 between PC2 and Ni abundance is not perfect. Nevertheless, when conducting a full analysis with
325 flight data, a more exact correspondence between PC2 and Ni abundance can be derived in order
326 to more accurately identify Ni abundances; this correspondence will be assisted by the direct and
327 complementary Ni elemental composition data from the GRS [*Lawrence et al.*, 2019]. Finally, all
328 of the meteoritic compositions contained no H, and as seen, their location within the PC data cloud
329 is near the top of the volume (Figure 5D, which is consistent with the fact that they contain no H).

330 As a final check to test the usefulness of this PC analysis, we simulated the expected count rate
331 of Mars crustal-like material [*Agee et al.*, 2013], which is relevant for the Psyche measurements
332 because we expect to measure neutron fluxes from Mars during the Mars gravity assist while en-
333 route to Psyche. These compositional values are also given in Table 2. While it is expected that
334 the flyby geometry will be near Mars’ equator, the longitudinal location is currently unknown as
335 it depends on parameters like the exact Psyche mission launch date, which will not be known until
336 it occurs. Nevertheless, Mars has a range of H concentrations across its equatorial region [*Maurice*
337 *et al.*, 2011], so we used six instances of Mars crustal-like compositions with variable H
338 concentrations ranging from 0.5 wt.% water equivalent hydrogen (WEH) to 9 wt.% WEH. The
339 PC-transformed neutron count rates are shown as dark-red symbols in Figure 5D, separately in
340 Figure 7 (PC3 versus WEH), and the values listed in Table 3. While Mars compositions are quite

341 different from the compositions considered in the original Psyche framework, they nevertheless
342 show good consistency. Specifically, based on our definition of silicate fraction, the Mars points
343 occur at low PC1 values, which is consistent with a high silicate fraction. Their PC2 values are
344 quite low, consistent with the low Ni abundances within the Mars composition. Finally, the major
345 variation is generally along the PC3 axis (Figure 7), which is consistent with the fact that the
346 primary compositional variation in the Mars compositions is due to H.

347

348 **5. Discussion and Summary**

349 Given the wide range of possible elemental compositions of asteroid Psyche, neutron
350 measurements from the asteroid include a high-energy epithermal neutron measurement to better
351 constrain its compositional nature and variability. Using validated particle transport simulations
352 with “artificial” compositions, we have shown that neutron flux variations due to metal-to-silicate,
353 Ni, and H variations can be uniquely distinguished using a principal component analysis.
354 Specifically, for our analysis PC1 was found to be sensitive to metal-to-silicate content, and PC2
355 was sensitive to Ni content. This same analysis has shown consistent results in distinguishing these
356 three compositional variabilities for possible Psyche-like meteorite compositions as well as Mars
357 compositions with variable H abundances.

358 As a first opportunity to test this framework, we note again that the Psyche mission is planning
359 to carry out a Mars gravity assist prior to reaching Psyche, where the spacecraft will pass within a
360 few hundred km of Mars’ surface. All spacecraft science instruments are planning to operate
361 through the gravity assist including the full GRNS. While not a required measurement, neutron
362 data acquired at Mars would provide useful anchor points for the eventual measurements at Psyche.
363 This is especially so because Mars’ surface is well characterized with prior neutron measurements
364 [*Maurice et al.*, 2011]. Thus, such Mars measurements could provide an early validation of the
365 analysis framework presented here, and possibly provide revisions to our understanding of the full
366 neutron data prior to reaching Psyche, should such revisions be necessary. We note that prior to
367 applying this framework, all the neutron data (either at Mars or Psyche) need to be fully corrected
368 for non-compositional observational variations as has been done in prior similar studies [*Maurice*
369 *et al.*, 2004; 2011; *Prettyman et al.*, 2012]

370 In summary, planetary neutron data have provided essential composition information at all
371 planetary bodies where such measurements have been made, e.g., the Moon, Mars, Mercury,

372 Vesta, and Ceres, which collectively span a wide range of iron, silicate, and H concentrations.
373 Given that so little is currently known about Psyche, it is important to have multiple, independent
374 ways to constrain its composition. GRNS neutron measurements will provide such compositional
375 constraints, namely a robust measure of the silicate fraction, as well as constraints on the Ni
376 fraction and surface H content.

377

378 **Acknowledgements:** The Psyche GRNS project is supported by the NASA Discovery Program
379 under contracts 1569206 from NASA Jet Propulsion Laboratory and 17-256 from Arizona State
380 University to the Johns Hopkins University Applied Physics Laboratory. Data archiving is
381 underway, and will be made available at <http://lib.jhuapl.edu/>.

382

Table 1. Variance and PC parameters

	Variance	C_{therm}	C_{LowEpi}	C_{HiEpi}	C_{fast}
PC1	0.953	-0.384	-0.168	-0.272	0.865
PC2	0.035	-0.817	-0.103	-0.304	-0.479
PC3	0.011	-0.429	0.309	0.838	0.133
PC4	0.0006	0.017	-0.930	0.362	-0.060

383

384

Table 2. Table of mass fraction abundances for six meteorite types and Mars compositions. These abundance values were taken from [Peplowski *et al.*, 2019].

	Iron	Pallasite	CB Chondrite	Mesosiderite	EH Chondrite	H Chondrite	Mars
H	0.0	0.0	0.0	0.0	0.0	0.0	5.87x10 ⁻⁴
C	0.0037	0.0	0.0	0.007	0.0039	0.0021	0.0
O	0.0	0.1722	0.129	0.214	0.3022	0.3533	0.4367
Na	0.0	0.0	0.0003	0.0009	0.0076	0.0	0.0291
Mg	0.0	0.1149	0.056	0.047	0.1101	0.1395	0.0494
Al	0.0	0.0	0.0063	0.021	0.0086	0.0105	0.0622
Si	0.0	0.0756	0.07	0.097	0.1731	0.1692	0.2332
P	0.0028	0.0030	0.0	0.0	0.0	0.0	0.0
S	0.0040	0.0089	0.0050	0.0270	0.0523	0.0198	0.0004
Cl	0.0	0.0	0.0	0.0	0.0	0.0	0.0023
K	0.0	0.0	0.0	0.0	0.0	0.0	0.0030
Ca	0.0	0.0011	0.0071	0.0148	0.0079	0.0121	0.0670
Ti	0.0	0.0	0.0	0.0	0.0	0.0	0.0062
Cr	0.0	0.0007	0.0030	0.0021	0.0032	0.0035	0.0013
Mn	0.0	0.0	0.0005	0.0016	0.0021	0.0023	0.0023
Fe	0.9170	0.5530	0.6740	0.5142	0.3113	0.2692	0.1060
Co	0.0046	0.0020	0.0022	0.0016	0.0008	0.0	0.0
Ni	0.0668	0.0685	0.0475	0.0510	0.0169	0.0169	0.0004
Sm	0.0	0.0	0.0	0.0	0.0	0.0	6.75x10 ⁻⁶
Eu	0.0	0.0	0.0	0.0	0.0	0.0	1.66x10 ⁻⁶
Gd	0.0	0.0	0.0	0.0	0.0	0.0	7.82x10 ⁻⁶
Th	0.0	0.0	0.0	0.0	0.0	0.0	2.76x10 ⁻⁶
U	0.0	0.0	0.0	0.0	0.0	0.0	5.38x10 ⁻⁷
Silicate fraction	0.016	0.376	0.273	0.429	0.669	0.712	0.894

386

387

388

389

390

391

392

Table 3. PC values for the six meteorite compositions and Mars compositions with five separate water equivalent hydrogen (WEH) concentrations.

	PC1	PC2	PC3
Iron	10.0	-2.20	5.97
Pallasite	2.19	-2.12	5.78
CB Chondrite	3.33	-2.05	5.58
Mesosiderite	1.79	-2.20	5.72
EH Chondrite	0.178	-2.80	5.78
H Chondrite	-0.273	-3.10	5.92
Mars (0.65 wt.% WEH)	-1.23	-4.80	7.52
Mars (0.9 wt.% WEH)	-1.23	-4.74	7.15
Mars (1.8 wt.% WEH)	-1.25	-4.58	6.52
Mars (4.5 wt.% WEH)	-1.33	-4.22	5.58
Mars (9.0 wt.% WEH)	-1.37	-3.77	4.75

393

394

395

396

397

398

399

400
401
402
403
404
405
406
407
408
409
410
411
412
413
414
415
416
417
418
419
420
421
422
423
424
425
426
427
428
429
430

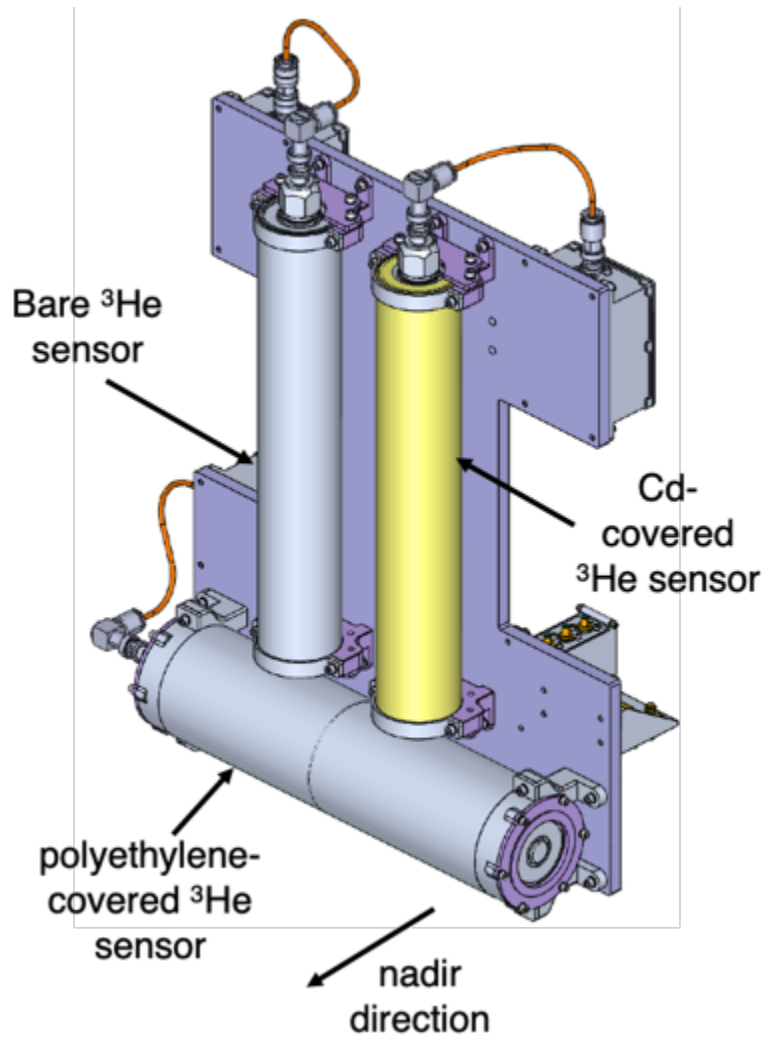


Figure 1. Psyche neutron spectrometer with three ^3He neutron sensors. The nadir direction that views Psyche is perpendicular to the cylinder axes of the sensors. Unlabeled components include pre-amplifier, high-voltage filter, harness connectors, and other instrument control functionality (e.g., thermal control). The length of each sensor assembly is ~ 30 cm.

431
432
433
434
435
436
437
438
439
440
441
442
443
444
445
446
447
448
449
450
451
452
453
454
455
456
457
458
459
460
461

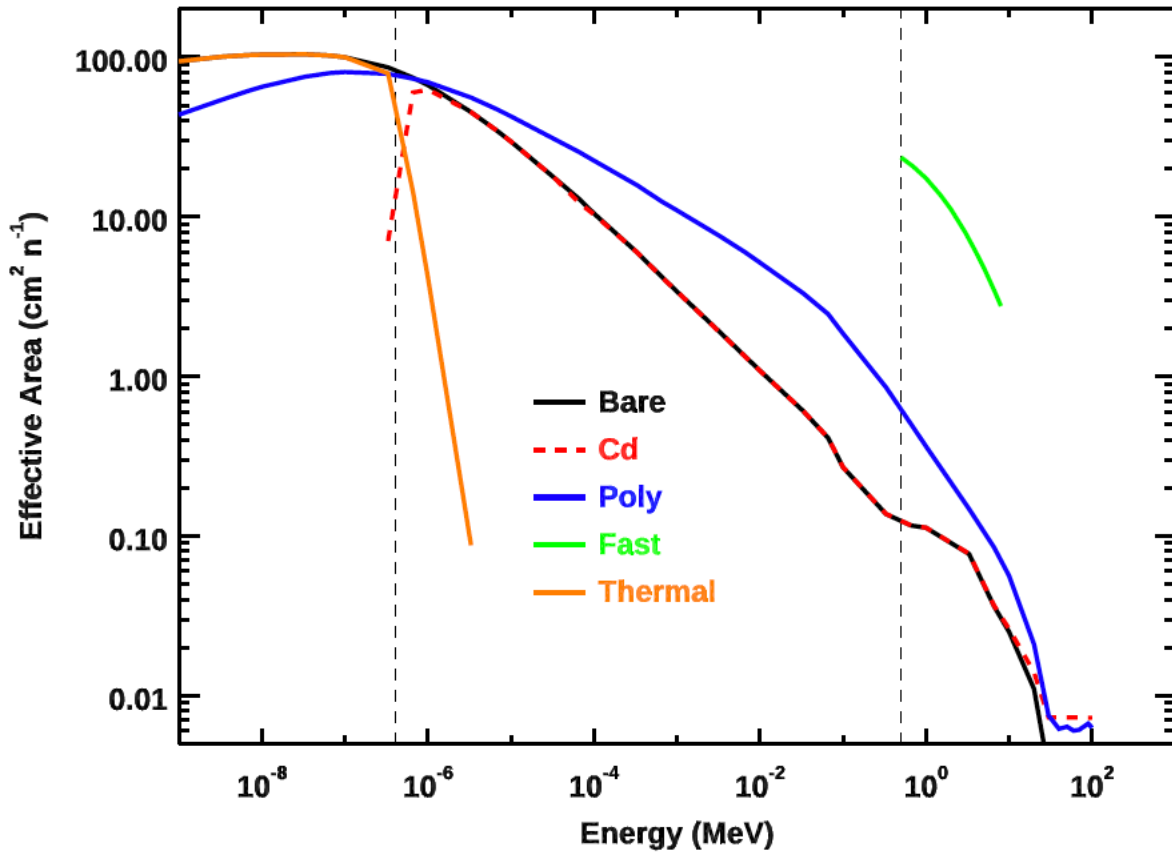


Figure 2. Modeled effective area (efficiency times area) for the four different neutron sensors that are part of the Psyche GRNS. The fast neutron effective-area is an estimate based on the efficiency calculated for the MESSENGER NS fast neutron sensor [Lawrence *et al.*, 2013a] combined with the cross-sectional area of the GRS AC shield (Section 3). The vertical, dashed lines indicate the standard energy boundaries for thermal to epithermal neutrons (0.4 eV), and epithermal to fast neutrons (0.5 MeV).

462
463
464
465
466
467
468
469
470
471
472
473
474
475
476
477
478
479
480
481
482
483
484
485
486
487
488
489
490
491
492

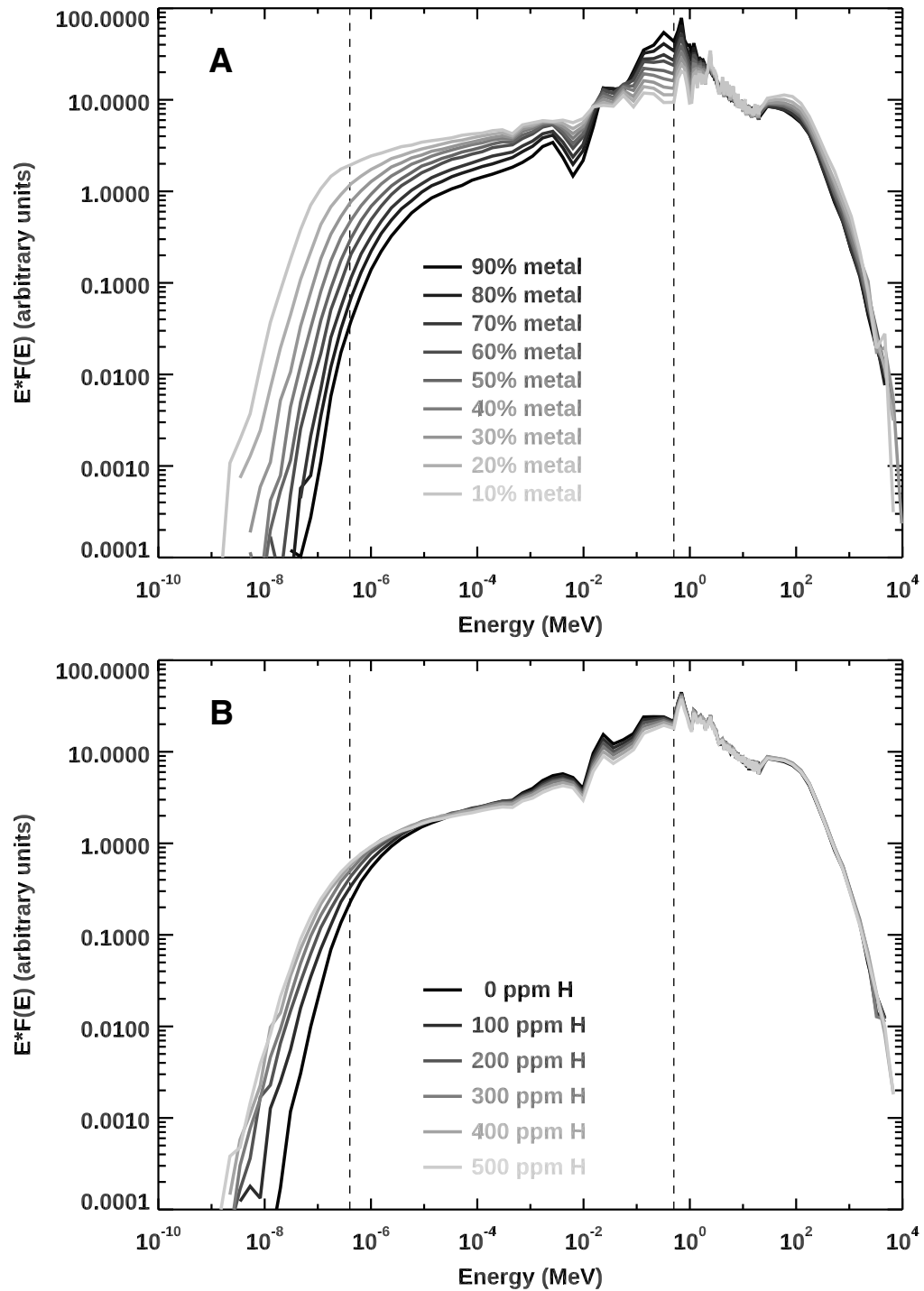
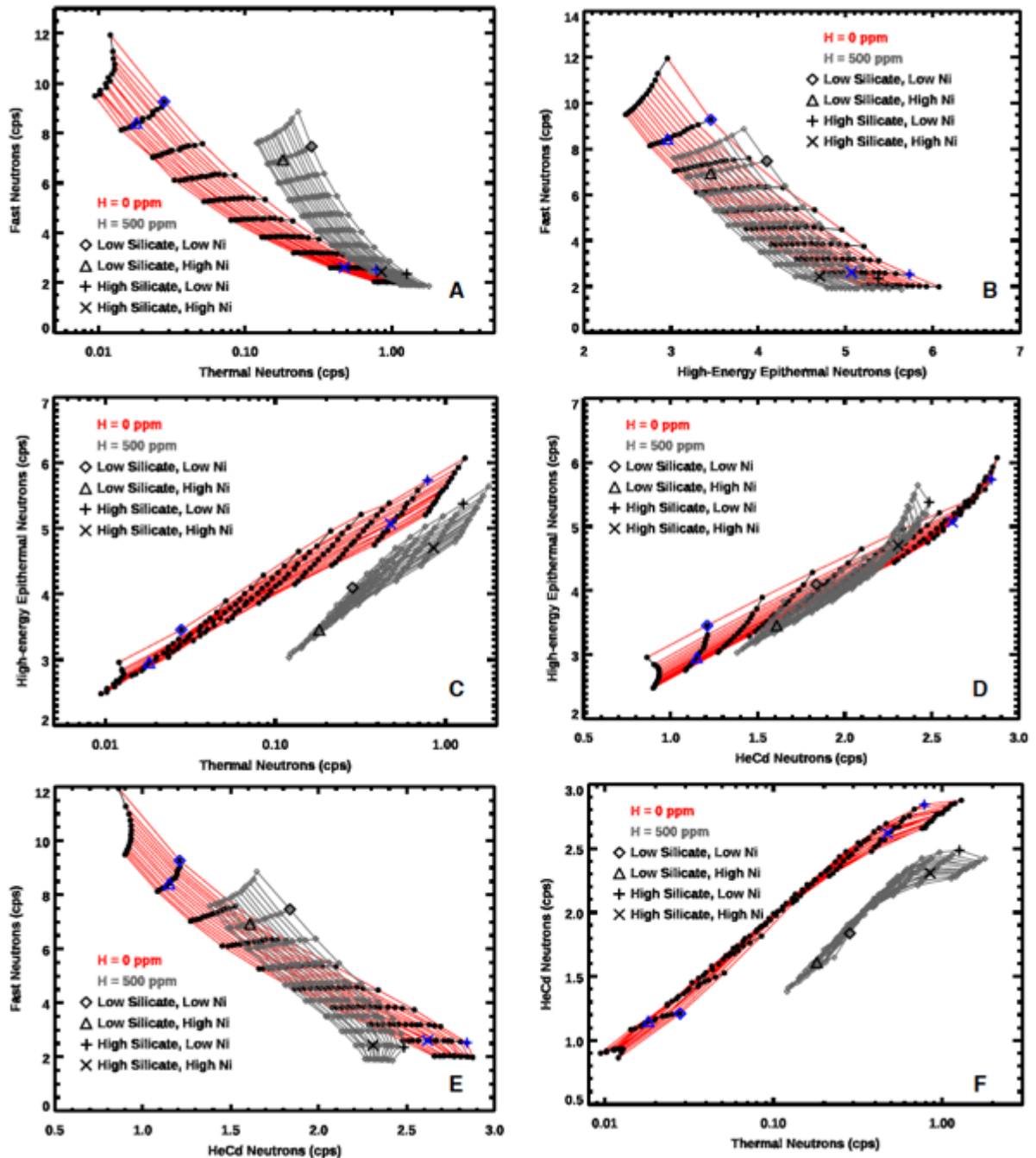


Figure 3. (A) Modeled neutron fluxes for range of metal-to-silicate compositions, with 8 wt.% Ni fraction within the metal; (B) and a range of hydrogen abundances within a metal-rich composition (0.9 metal fraction and 2 wt.% Ni within the metal). The vertical, dashed lines indicate the standard energy boundaries for thermal to epithermal neutrons (0.4 eV), and epithermal to fast neutrons (0.5 MeV).

493
 494
 495
 496
 497
 498
 499
 500
 501
 502
 503
 504
 505
 506
 507
 508
 509
 510
 511
 512
 513
 514
 515
 516
 517



518 **Figure 4.** Simulated count-rate “feather plots” for all permutations of the four neutron measurements
 519 (A–F). 840 separate simulations were completed for a phase space of possible Psyche compositions
 520 ranging from 10 to 90 vol% silicates (or pyroxene), 2 to 30 wt.% Ni, and 0 to 500 ppm H. Contours
 521 of constant Ni abundances are given by the red lines; contours of constant silicate content are given
 522 by the black lines. Illustrative combinations of low silicate (20 vol. %), high silicate (80 vol.%), low
 523 Ni (2 wt.%) and high Ni (20 wt.%) are given by the symbols. The red and black feather plots use 0
 ppm H, and the gray feather plots use 500 ppm H.

524
525
526
527
528
529
530
531
532
533
534
535
536
537
538
539
540
541
542
543
544
545
546
547
548
549
550
551
552
553
554

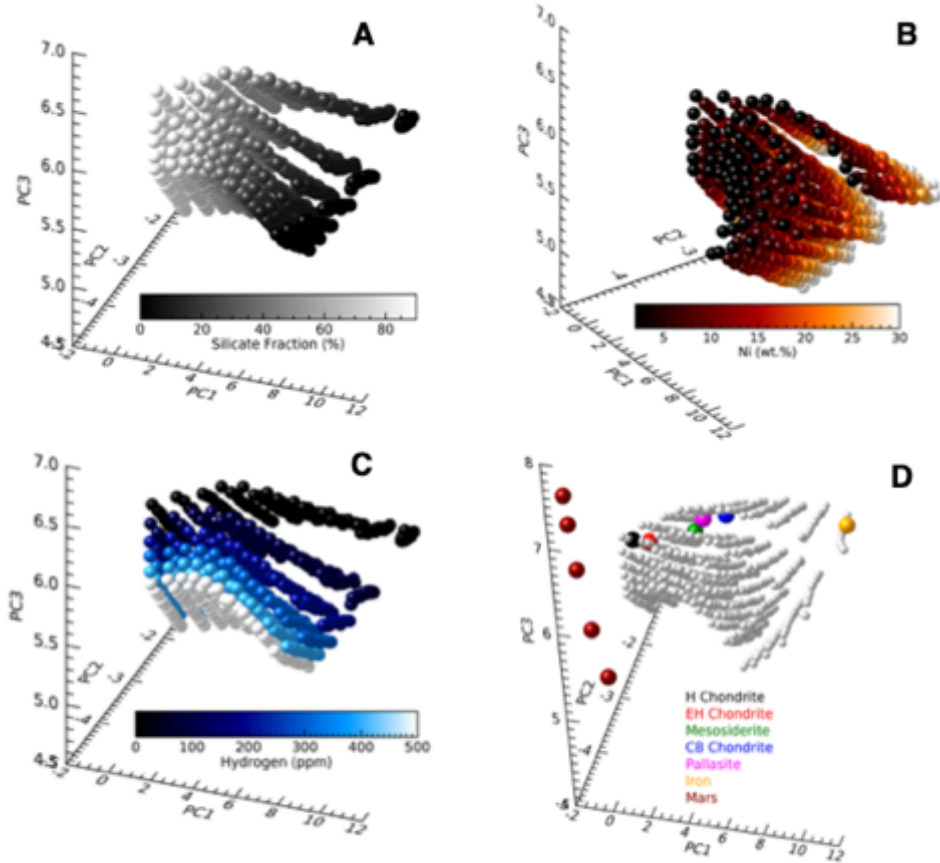


Figure 5. Three-dimensional scatterplot of the three principal components for the 840 neutron simulations for the range of silicate fraction, Ni concentrations, and hydrogen concentrations. While the axes rotations are different, the data points are in same locations for all panels. Data points are color coded based on silicate fraction (A), Ni concentration (B), and H concentration (C). Panel (D) shows the principal components for six different meteorite compositions (Table 2) along with six versions of Mars compositions with H concentrations of 0.5 wt.% (nominal value in Table 2), 0.9 wt.%, 1.8 wt.%, 4.5 wt.%, and 9 wt.% water equivalent hydrogen (WEH). Increasing values of WEH range from high to low PC3 values.

555
556
557
558
559
560
561
562
563
564
565
566
567
568
569
570
571
572
573
574
575
576
577
578
579
580
581
582
583
584
585

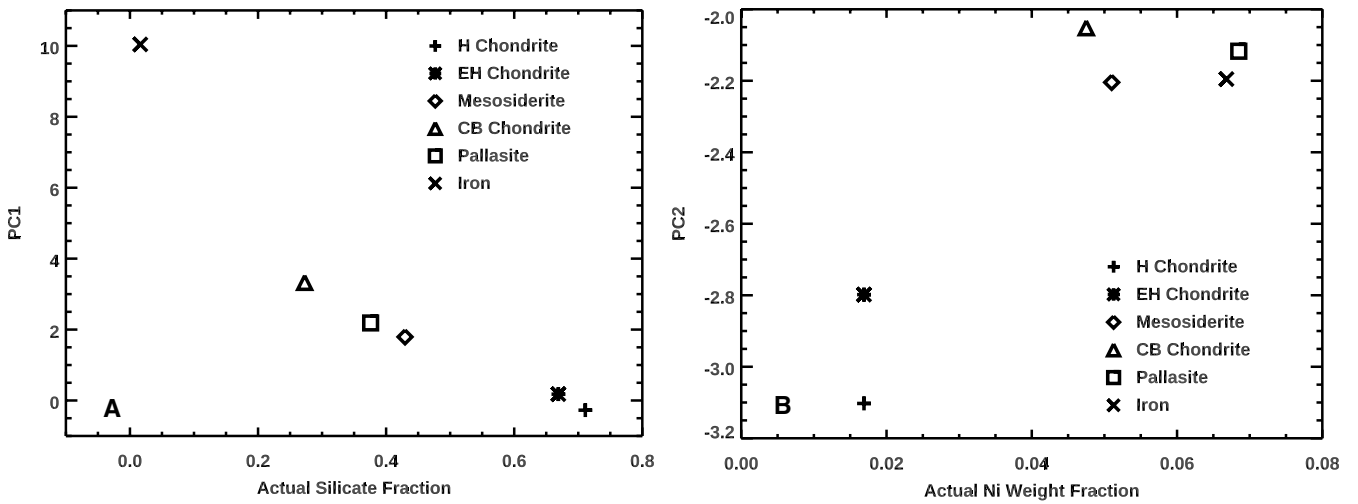


Figure 6. PC1 versus actual silicate values (A), and PC2 versus actual Ni concentrations for the six meteorite compositions given in Table 2.

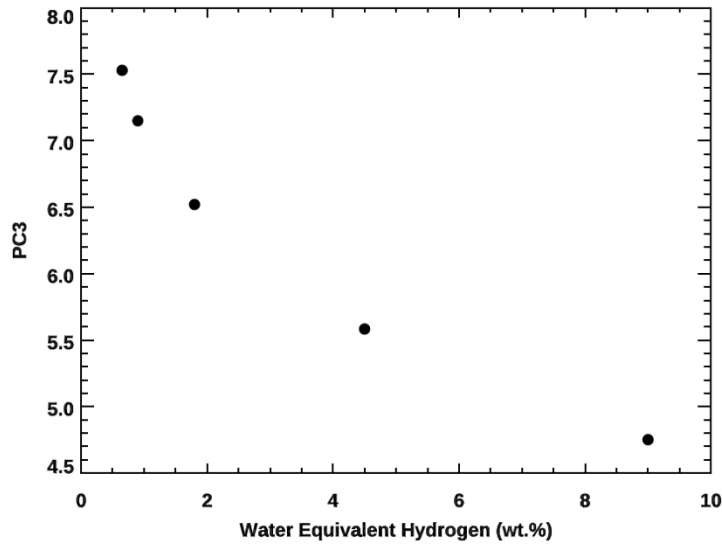


Figure 7. PC3 versus actual water equivalent hydrogen abundances for the five different Mars compositions shown in Figure 5D.

586

587 **References:**

588 Agee, C. B., et al. (2013), Unique Meteorite from Early Amazonian Mars: Water-Rich Basaltic
589 Breccia Northwest Africa 7034, *Science*, 339(6121), 780-785, doi:10.1126/science.1228858.

590 Beck, A. W., D. J. Lawrence, P. N. Peplowski, T. H. Prettyman, T. J. McCoy, H. Y. McSween,
591 M. J. Toplis, and N. Yamashita (2015), Using HED meteorites to interpret neutron and gamma-
592 ray data from asteroid 4 Vesta, *Meteoritics & Planetary Science*, 50(8), 1311-1337,
593 doi:10.1111/maps.12467.

594 Berlin, J., R. H. Jones, A. J. Brearley, and M. N. Spilde (2008), Determining Bulk Chemical
595 Compositions of Chondrules by Electron Microprobe: Modal Recombination versus Defocused
596 Beam Analyses, *Microscopy and Microanalysis*, 14, 110 - 111, doi:10.1017/S1431927608084845.

597 Chevrel, S., P. Pinet, Y. Daydou, S. Maurice, D. Lawrence, W. Feldman, and P. Lucey (2002),
598 Integration of the Clementine UV-VIS spectral reflectance data and the Lunar Prospector gamma-
599 ray spectrometer data: A global-scale multielement analysis of the lunar surface using iron,
600 titanium, and thorium abundances, *Journal of Geophysical Research-Planets*, 107(E12),
601 doi:10.1029/2000JE001419.

602 Elkins-Tanton, L. T., et al. (2020), Observations, Meteorites, and Models: A Preflight Assessment
603 of the Composition and Formation of (16) Psyche, *Journal of Geophysical Research-Planets*,
604 125(3), doi:10.1029/2019je006296.

605 Elphic, R. C., D. J. Lawrence, W. C. Feldman, B. L. Barraclough, S. Maurice, A. B. Binder, and
606 P. G. Lucey (2000), Lunar rare earth element distribution and ramifications for FeO and TiO₂ :
607 Lunar Prospector neutron spectrometer observations, *Journal of Geophysical Research*, 105(E8),
608 20333-20333, doi:10.1029/1999JE001176.

609 Feldman, W., et al. (2004), Gamma-Ray, Neutron, and Alpha-Particle Spectrometers for the Lunar
610 Prospector mission, *Journal of Geophysical Research: Planets*, 109(E7),
611 doi:10.1029/2003JE002207.

612 Feldman, W. C., B. L. Barraclough, S. Maurice, R. C. Elphic, D. J. Lawrence, D. R. Thomsen, and
613 A. B. Binder (1998a), Major compositional units of the moon: Lunar prospector thermal and fast
614 neutrons, *Science*, 281(5382), 1489-1493, doi:10.1126/science.281.5382.1489.

615 Feldman, W. C., S. Maurice, A. B. Binder, B. L. Barraclough, R. C. Elphic, and D. J. Lawrence
616 (1998b), Fluxes of fast and epithermal neutrons from Lunar Prospector: Evidence for water ice at
617 the lunar poles, *Science*, 281(5382), 1496-1500, doi:10.1126/science.281.5382.1496.

618 Feldman, W. C., M. T. Mellon, O. Gasnault, B. Diez, R. C. Elphic, J. J. Hagerty, D. J. Lawrence,
619 S. Maurice, and T. H. Prettyman (2007), Vertical distribution of hydrogen at high northern
620 latitudes on Mars: The Mars Odyssey Neutron Spectrometer, *Geophysical Research Letters*, 34(5),
621 doi:10.1029/2006gl028936.

622 Feldman, W. C., A. Pathare, S. Maurice, T. H. Prettyman, D. J. Lawrence, R. E. Milliken, and B.
623 J. Travis (2011), Mars Odyssey neutron data: 2. Search for buried excess water ice deposits at
624 nonpolar latitudes on Mars, *Journal of Geophysical Research-Planets*, 116,
625 doi:10.1029/2011JE003806.

626 Gasnault, O., W. C. Feldman, S. Maurice, I. Genetay, C. d'Uston, T. H. Prettyman, and K. R.
627 Moore (2001), Composition from fast neutrons: Application to the Moon, *Geophysical Research*
628 *Letters*, 28(19), 3797-3800, doi:10.1029/2001GL013072.

629 Hardersen, P. S., M. J. Gaffey, and P. A. Abell (2005), Near-IR spectral evidence for the presence
630 of iron-poor orthopyroxenes on the surfaces of six M-type asteroids, *Icarus*, 175(1), 141-158,
631 doi:10.1016/j.icarus.2004.10.017.

632 Lawrence, D. J., W. C. Feldman, R. C. Elphic, J. J. Hagerty, S. Maurice, G. W. McKinney, and T.
633 H. Prettyman (2006), Improved modeling of Lunar Prospector neutron spectrometer data:
634 Implications for hydrogen deposits at the lunar poles, *Journal of Geophysical Research*, 111(E8),
635 E08001, doi:10.1029/2005JE002637.

636 Lawrence, D. J., V. R. Eke, R. C. Elphic, W. C. Feldman, H. O. Funsten, T. H. Prettyman, and L.
637 F. A. Teodoro (2011), Technical comment on "Hydrogen mapping of the lunar South Pole using

638 the LRO neutron detector experiment LEND", *Science*, 334(6059), 1058,
639 doi:10.1126/science.1203341.

640 Lawrence, D. J., et al. (2013a), Evidence for water ice near Mercury's north pole from
641 MESSENGER Neutron Spectrometer measurements, *Science*, 339(6117), 292-296,
642 doi:10.1126/science.1229953.

643 Lawrence, D. J., P. N. Peplowski, T. H. Prettyman, W. C. Feldman, D. Bazell, D. W. Mittlefehldt,
644 R. C. Reedy, and N. Yamashita (2013b), Constraints on Vesta's elemental composition: Fast
645 neutron measurements by Dawn's gamma ray and neutron detector, *Meteoritics & planetary*
646 *science*, 48(11), 2271-2288, doi:10.1111/maps.12187.

647 Lawrence, D. J., P. N. Peplowski, A. W. Beck, W. C. Feldman, E. A. Frank, T. J. McCoy, L. R.
648 Nittler, and S. C. Solomon (2017), Compositional terranes on Mercury: Information from fast
649 neutrons, *Icarus*, 281, 32-45, doi:10.1016/j.icarus.2016.07.018.

650 Lawrence, D. J., et al. (2019), The Psyche Gamma-Ray and Neutron Spectrometer: Update on
651 Instrument Design and Measurement Capabilities, in *50th Lunar and Planetary Science*
652 *Conference*, edited, p. Abstract #1544, Houston, Texas.

653 Lingenfelter, R. E., W. N. Hess, and E. H. Canfield (1961), Lunar Neutron Flux, *Journal of*
654 *Geophysical Research*, 66(9), 2665-2671, doi:10.1029/JZ066i009p02665.

655 Maurice, S., D. J. Lawrence, W. C. Feldman, R. C. Elphic, and O. Gasnault (2004), Reduction of
656 neutron data from Lunar Prospector, *Journal of Geophysical Research*, 109(E7), E07S04,
657 doi:10.1029/2003JE002208.

658 Maurice, S., W. Feldman, B. Diez, O. Gasnault, D. J. Lawrence, A. Pathare, and T. Prettyman
659 (2011), Mars Odyssey neutron data: 1. Data processing and models of water-equivalent-hydrogen
660 distribution, *Journal of Geophysical Research*, 116(E11), E11008-E11008,
661 doi:10.1029/2011JE003810.

662 Peplowski, P. N., D. Bazell, L. G. Evans, J. O. Goldsten, D. J. Lawrence, and L. R. Nittler (2015a),
663 Hydrogen and major element concentrations on 433 Eros: Evidence for an L- or LL-chondrite-like
664 surface composition, *Meteorit. Planet. Sci.*, 50(3), 353-367, doi:10.1111/maps.12434.

665 Peplowski, P. N., D. J. Lawrence, W. C. Feldman, J. O. Goldsten, D. Bazell, L. G. Evans, J. W.
666 Head, L. R. Nittler, S. C. Solomon, and S. Z. Weider (2015b), Geochemical terranes of Mercury's
667 northern hemisphere as revealed by MESSENGER neutron measurements, *Icarus*, 253, 346-363,
668 doi:10.1016/j.icarus.2015.02.002.

669 Peplowski, P. N., D. J. Lawrence, A. W. Beck, M. Burks, N. L. Chabot, J. O. Goldsten, J. Wilson,
670 and Z. Yokley (2018), Nuclear Spectroscopy of Asteroid 16 Psyche, in *49th Lunar and Planetary*
671 *Science Conference*, edited, p. Abstract #2114, Houston, TX.

672 Peplowski, P. N., T. J. McCoy, M. Liebel, A. W. Beck, M. T. Burks, L. T. Elkins-Tanton, D. J.
673 Lawrence, and T. H. Prettyman (2019), Gamma-Ray Spectroscopy of Metal-Rich Meteorites:
674 Preparations for The Psyche Gamma-Ray Spectroscopy Investigation, in *50th Lunar and*
675 *Planetary Science Conference*, edited, p. Abstract #1731, Houston, Texas.

676 Peplowski, P. N., and K. Stockstill-Cahill (2019), Analytical Identification and Characterization
677 of the Major Geochemical Terranes of Mercury's Northern Hemisphere, *Journal of Geophysical*
678 *Research-Planets*, 124(9), 2414-2429, doi:10.1029/2019JE005997.

679 Peplowski, P. N., Z. W. Yokley, M. Liebel, S. Cheng, R. C. Elphic, S. F. Hoogerheide, D. J.
680 Lawrence, and J. S. Nico (2020), Position-dependent neutron detection efficiency loss in He-3 gas
681 proportional counters, *Nuclear Instruments & Methods in Physics Research Section a-*
682 *Accelerators Spectrometers Detectors and Associated Equipment*, 982,
683 doi:10.1016/j.nima.2020.164574.

684 Prettyman, T. H., J. J. Hagerty, R. C. Elphic, W. C. Feldman, D. J. Lawrence, G. W. McKinney,
685 and D. T. Vaniman (2006), Elemental composition of the lunar surface: Analysis of gamma ray
686 spectroscopy data from Lunar Prospector, *Journal of Geophysical Research*, 111(E12), E12007-
687 E12007, doi:10.1029/2005JE002656.

688 Prettyman, T. H., et al. (2012), Elemental Mapping by Dawn Reveals Exogenic H in Vesta's
689 Regolith, *Science*, 338(6104), 242-246, doi:10.1126/science.1225354.

690 Prettyman, T. H., et al. (2013), Neutron absorption constraints on the composition of 4 Vesta,
691 *Meteorit. Planet. Sci.*, 48(11), 2211-2236, doi:10.1111/maps.12244.

692 Prettyman, T. H., et al. (2017), Extensive water ice within Ceres' aqueously altered regolith:
693 Evidence from nuclear spectroscopy, *Science*, 355(6320), 55-58, doi:10.1126/science.aah6765.

694 Reddy, V., D. J. Lawrence, L. T. Elkins-Tanton, and D. Takir (2018), Constraining Hydrogen
695 Abundance on Asteroid (16) Psyche, in *49th Lunar and Planetary Science Conference*, edited, p.
696 Abstract #1344, Houston, Texas.

697 Sanchez, J. A., V. Reddy, M. K. Shepard, C. Thomas, E. A. Cloutis, D. Takir, A. Conrad, C.
698 Kiddell, and D. Applin (2017), Detection Of Rotational Spectral Variation On The M-Type
699 Asteroid (16) Psyche, *Astron. J.*, 153(1), doi:10.3847/1538-3881/153/1/29.

700 Takir, D., V. Reddy, J. A. Sanchez, M. K. Shepard, and J. P. Emery (2017), Detection Of Water
701 And/Or Hydroxyl On Asteroid (16) Psyche, *Astron. J.*, 153(1), doi:10.3847/1538-3881/153/1/31.

702 Wilks, D. S. (2011), *Statistical Methods in the Atmospheric Sciences, Third Edition*, 676 pp.,
703 Academic Press, Amsterdam, The Netherlands.

704 Wilson, J. T., D. J. Lawrence, P. N. Peplowski, and W. C. Feldman (2019), MESSENGER Gamma
705 Ray Spectrometer and Epithermal Neutron Hydrogen Data Reveal Compositional Differences
706 Between Mercury's Hot and Cold Poles, *Journal of Geophysical Research-Planets*, 124(3), 721-
707 733, doi:10.1029/2018je005871.

708 Yamashita, N., et al. (2013), Distribution of iron on Vesta, *Meteoritics & Planetary Science*,
709 48(11), 2237-2251, doi:10.1111/maps.12139.

710